Orbitally driven giant phonon anharmonicity in SnSe

C. W. Li[1†], J. Hong[1†], A. F. May[1], D. Bansal[1], S. Chi[2], T. Hong[2], G. Ehlers[2] and O. Delaire[1*]

Understanding elementary excitations and their couplings in condensed matter systems is critical for developing better energy-conversion devices. In thermoelectric materials, the heat-to-electricity conversion efficiency is directly improved by suppressing the propagation of phonon quasiparticles responsible for macroscopic thermal transport. The current record material for thermoelectric conversion efficiency, SnSe, has an ultralow thermal conductivity, but the mechanism behind the strong phonon scattering remains largely unknown. From inelastic neutron scattering measurements and first-principles simulations, we mapped the four-dimensional phonon dispersion surfaces of SnSe, and found the origin of the ionic-potential anharmonicity responsible for the unique properties of SnSe. We show that the giant phonon scattering arises from an unstable electronic structure, with orbital interactions leading to a ferroelectric-like lattice instability. The present results provide a microscopic picture connecting electronic structure and phonon anharmonicity in SnSe, and offers new insights on how electron–phonon and phonon–phonon interactions may lead to the realization of ultralow thermal conductivity.

Interactions of phonon quasiparticles with electronic, spin, or orbital degrees of freedom can lead to unusual bulk thermodynamic and transport phenomena, such as superconductivity, charge-density waves, multiferroicity, or soft-mode phase transitions. Such couplings in metal chalcogenides have been of particular interest in thermoelectrics, quasi-two-dimensional layered systems, Fe-based superconductors, and topological insulators. Thermoelectric materials and devices, which are of great interest for sustainable power generation applications, require tuning of quasiparticle transport to achieve a low lattice thermal conductivity while maintaining a high electrical conductivity[1,2]. A variety of approaches are used to suppress the contribution of phonons (lattice vibrations) to the thermal conductivity, including nanostructuring, using large unit cells with many optical phonon branches, scattering acoustic phonons with 'rattling' atoms, leveraging anisotropic layered structures, or coupling to electronic instabilities[1–11]. Systems with intrinsically strong anharmonicity in their lattice potential open up opportunities to decouple phonon and electron transport, without requiring artificial nanostructuring, alleviating concerns of device cost and longevity. They also present avenues for fundamental studies of how many-body phonon–phonon interactions disrupt the classical phonon gas picture[12–14]. However, outstanding questions remain on how to tune electronic and orbital degrees of freedom to realize strongly coupled phonon systems with good thermoelectric performance.

Tin selenide (SnSe) was recently reported to achieve a record-high figure of merit $zT > 2$ along specific crystallographic directions, by exploiting a significant anisotropy in both electrical and thermal transport properties, and a very low lattice thermal conductivity, $\kappa_{lat} < 1\,W\,m^{-1}\,K^{-1}$ at ambient temperature[15–18]. The decrease of κ_{lat} with increasing temperature for all crystallographic directions also suggests that lattice anharmonicity is an important phonon scattering mechanism in this compound[15,17,19]. However, the electronic origin of this strong anharmonicity, and which phonon modes are involved, remained uncertain. Understanding phonon propagation velocities and linewidths (phonon scattering

rates) is critical to gain definitive insights into the dominant processes accounting for the very low thermal conductivity. Inelastic neutron scattering (INS) measurements on single crystals have been proved to be powerful in resolving momentum-dependent phonon dispersions, and thus provide critical information to rationalize anisotropic thermal transport[6–9,12,14]. Here, we report decisive comprehensive measurements of phonon dispersions as a function of temperature in single crystals of SnSe using INS, and analysis with first-principles simulations of phonons, including anharmonic effects. Strikingly, our measurements directly reveal a lattice instability associated with the condensation of a soft transverse optic (TO) phonon mode. With simulations, we show how the strong underlying anharmonicity stems from a bonding instability and results in temperature-dependent force constants. The instability arises from the long-range resonant p-bond network of Se atoms, coupled to stereochemically active Sn $5s$ orbitals.

Single crystals of SnSe were synthesized with high-purity Sn and Se (Alfa Aesar, 99.999%), using a modified Bridgman technique (details in Methods) and checked with X-ray and neutron diffraction. The crystal structure is illustrated in Fig. 1 and Supplementary Fig. I. Typical crystals used in neutron experiments had a mass of approximately 8 g. INS measurements were performed on single crystals with the high-resolution CNCS spectrometer at the Spallation Neutron Source (SNS). The four-dimensional scattering function, $S(\mathbf{Q}, E)$, was mapped at $T = 100$, 300, 486 and 648 K (approximately 50 Brillouin zones at each temperature), using an incident energy $E_i = 12$ meV (details in Methods). The data were subsequently 'sliced' along selected $\mathbf{Q}$-directions in reciprocal space to produce two-dimensional views of dispersions. We denote $\mathbf{Q} = \mathbf{q} + \boldsymbol{\tau}$, with $\mathbf{Q}$ the neutron wavevector transfer, $\mathbf{q}$ the phonon wavevector, and $\boldsymbol{\tau}$ a reciprocal lattice vector. Slices revealing transverse modes for $\mathbf{Q}$ along $[H,0,2]$ and $[0,K,2]$ at $T = 100$ and 648 K are shown in Fig. 2. First-principles simulations were performed with density-functional theory (DFT) as implemented in VASP, using both local-density approximation (LDA) and generalized gradient approximation (GGA) exchange–correlation
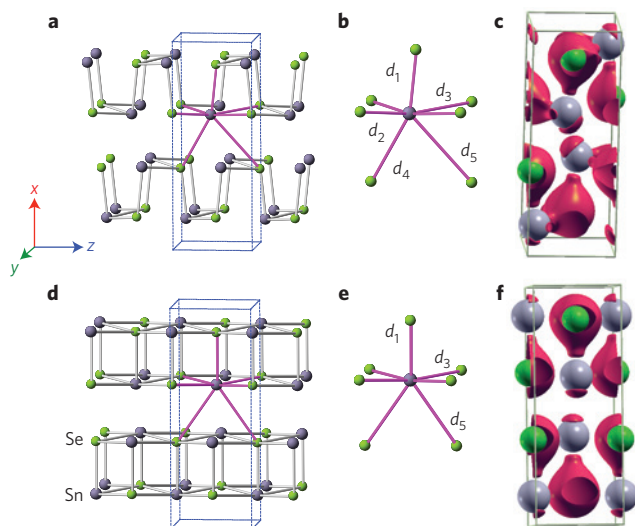
Figure 1 | Illustration of structural distortion across the *Cmcm–Pnma* transition in SnSe and the corresponding electronic densities. a,d, Crystal structures of SnSe in the *Pnma* (**a**) and *Cmcm* (**d**) phase (conventional non-primitive cell for the latter), showing the double bilayer structure and *Pnma* distortion. **b,e,** Sn coordination polyhedron corresponding to the structures in **a,d**, respectively. **c,f,** Valence electron density (isosurface at 0.26 e Å^{-3}), computed from first principles for the structures in **a,d**, respectively. Sn atoms are in grey and Se atoms in green. The Sn $5s^2$ lone pairs are seen as 'caps' in the space between bilayers.

functionals (details in Methods). Lattice parameters predicted with both LDA and GGA were in good agreement with reported values (Supplementary Table I)[20], whereas LDA achieved better agreement with INS measurements for phonons. The LDA phonon dispersions and polarization vectors were computed with Phonopy[21], from which we computed $S(\mathbf{Q}, E)$ via Supplementary Equation I, then convolved with the CNCS instrumental resolution (details in Methods). Computed $S(\mathbf{Q}, E)$ slices for $[H,0,2]$ and $[0,K,2]$ are plotted in Fig. 2a,b, and compared with INS data at $T = 100$ K in Fig. 2c,d, showing excellent agreement for both the phonon energies and INS intensities. Additional results for measured and computed $S(\mathbf{Q}, E)$ slices in other directions are shown in Supplementary Fig. II. The transverse acoustic and optic phonons in Fig. 2 reveal critical aspects of the lattice dynamics of SnSe leading to the ultralow thermal conductivity, as detailed below.

As can be seen in Fig. 2, $S(\mathbf{Q}, E)$ slices along $[H,0,2]$ and $[0,K,2]$ reveal transverse acoustic (TA) and TO phonons propagating along Γ–X and Γ–Y, respectively, both polarized along the *c*-axis (direction of atomic motions). Strikingly, we find that the TA modes (emanating from the Bragg peaks at $E = 0$ meV) are considerably softer along the Γ–X direction than along Γ–Y. The anisotropy is also seen in Supplementary Figs II and III. This is compatible with κ_{lat} being much lower along the *a*-axis, across the layers, than within the plane of the layers (*b*–*c* plane)[15–18]. Our computations attribute this effect to weak interlayer bonding (long $d_{4,5}$ bonds in Fig. 1b). In addition, along Γ–X, the *c*-polarized TA branch exhibits a characteristic band-folding at the X-point, with the acoustic branch folded back into a TO branch when reaching the Brillouin zone boundary (at half-integer H values, denoted by thin vertical lines in Fig. 2c,e). As a result, the dispersions along Γ–X resemble two sets of overlapping 'arch-like' acoustic branches. This band-folding is also observed in simulations (Fig. 2a). This results in a very low TO branch, whose energy at the zone centre is only about 4 meV at 100 K. In sharp contrast, this lowest TO$_c$ branch disperses upwards steeply in the Γ–Y direction, leading to an unusual saddle point in the dispersion surface (the zone centre is the same in both left and
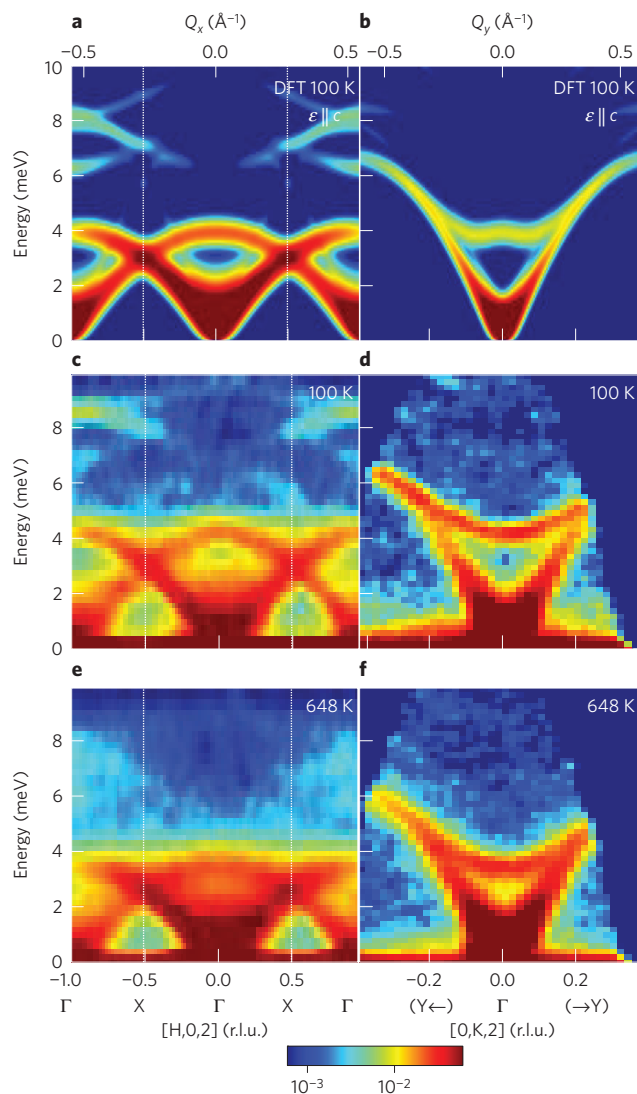
Figure 2 | INS measurements and first-principles simulations reveal the strong dispersion anisotropy and softening with temperature of the low-energy optic phonons. a,b, $S(\mathbf{Q}, E)$ calculated from first principles for the same directions, populated at $T = 100$ K, showing good agreement with INS data. **c,d,** Phonon dynamical structure factor, $S(\mathbf{Q}, E)$ measured with INS for momenta along $[H,0,2]$ and $[0,K,2]$ (reciprocal lattice units—r.l.u.) at 100 K. **e,f,** Same as **c,d** but at 648 K.

right panels). It is important that both TO and TA branches along Γ–Y are much stiffer than along Γ–X, accounting for anisotropic thermal transport. Furthermore, Fig. 2e,f also reveals a drastic softening of phonon dispersions along Γ–X at higher temperature ($T = 648$ K), compared to a much more modest softening of TA$_c$ modes along Γ–Y. Thus, the degree of anharmonicity of phonons also exhibits a strong anisotropy (not just the dispersions). We discuss below the origin of this striking effect.

We now relate the anisotropy in dispersions and the softening to the crystallography of SnSe. The atomic arrangement of SnSe has a layered orthorhombic structure, with two Sn–Se bilayers in the unit cell along the *a*-direction, as illustrated in Fig. 1a. The crystal structure is *Pnma* below $T_c \approx 810$ K (refs 20,22,23) (here we follow the crystallographic notation of ref. 20). Heating above T_c, the system transforms to a higher-symmetry orthorhombic (*Cmcm*) structure (Fig. 1d, conventional cell), which preserves the bilayer stacking, but in which the Sn coordination environment gains higher symmetry, as seen in Fig. 1b,e (refs 20,22,23). The

Table 1 | Comparison between Raman/infrared and INS measurements of zone-centre optical modes.

Phonon mode	Raman/IR* RT	INS E (width) (meV)			
	E (meV)	100 K	300 K	486 K	648 K
A_g	4.1	4.47 (0.24)	4.25 (0.15)	3.94 (0.16)	3.66 (0.30)
B_{3g}	4.6	4.79 (0.10)	4.57 (0.10)	4.34 (0.18)	4.17 (0.37)
B_{3g}	Inactive	6.09†	5.89†	5.56 (0.24)	5.28 (0.30)
B_{1g}	7.1	7.27†	6.99 (0.19)	6.73 (0.28)	6.54 (0.41)
A_g	8.8	8.88 (0.16)	8.51 (0.27)	8.00 (0.45)	7.60 (0.48)
B_{2g}	Inactive	8.88 (0.20)	8.67 (0.22)	8.60 (0.33)	8.36 (0.56)

Linewidths from INS (in parentheses) are corrected for instrument resolution. *Ref. 32. †Resolution limited.

high-T $Cmcm$ and low-T $Pnma$ phases are related by an 'accordion-like' distortion on cooling, corresponding to a distortion of the local Sn coordination polyhedron, and corrugating the bilayers along the c-direction[20]. In Supplementary Fig. I, we compare our results for the temperature dependence of lattice parameters with values from the literature[20]. As can be seen in this figure, the evolution of lattice parameters and bond distances is continuous across the phase transition, indicating that the transition is second order (compatible with the group–subgroup relationship of the respective space groups—$Cmcm$: 63, $Pnma$: 62), with the primary-order parameter corresponding to the Sn motion along c (ref. 22). However, the connection between this displacive phase transition and the lattice dynamics has never been previously observed, to our knowledge. Our temperature-dependent INS measurements and simulations show how the atomic motions associated with the transition are strongly anharmonic, impacting thermal transport, and directly reveal that the $Pnma \rightarrow Cmcm$ transition results from the condensation of an A_g-symmetry soft mode at the zone centre.

The detailed temperature dependence at important **Q** points was measured using the HB-3 triple-axis spectrometer (thermal neutrons, $E_f = 14.7$ meV) at the High Flux Isotope Reactor (details in Methods). Spectra for the TO_c mode near the $(0,0,2)$ zone-centre (**Q** $= [0, 0, 1.95]$) and the zone-boundary TA_c mode at X (**Q** $= [0.5, 0, 2]$), both c-polarized, are shown in Fig. 3a,b for $300 \leq T \leq 850$ K. These constant-**Q** spectra are also compared with spectra extracted from the CNCS data at the same wavevectors, showing excellent agreement. The zone-centre data from CNCS and the fitted temperature-dependent phonon energies are shown in Fig. 3c–e. As can be seen in 3a, the TO_c at Γ undergoes a marked softening between 500 K and 750 K. Close to the transition $775\,\text{K} < T < 825\,\text{K}$, the mode seems fully damped and merges with the low-energy TA peak close to the Bragg peak. Some stiffening is observed on further heating in the $Cmcm$ phase ($T = 825$, 850 K). This temperature dependence of the lowest TO_c mode near **q** $= 0$ is characteristic of soft-mode instabilities[24,25], and indeed our simulations confirm that this mode has the A_g-symmetry of the soft mode expected for this phase transition[22]. Moreover, as can be seen in Fig. 2c,e, both the TA_c and TO_c branches along Γ–X exhibit a very pronounced softening at 648 K. This strong softening (about 20%) affects the entire TA–TO manifold along Γ–X (from 4.5 meV to 3.6 meV for TO_c at Γ). This behaviour can be contrasted with the TA_c along Γ–Y, which softens much less (about 10%). As a result, along Γ–Y, the TO_c branch develops an extended overlap with the TA_c branch as T increases. The energies and linewidths of six low-energy TO modes are listed in Table 1, showing their softening and broadening with temperature. Table 2 lists acoustic group velocities and their temperature dependence. From 100 to 648 K, the TA_a velocities decrease by 11% and 9% on average along Γ–Y and Γ–Z, respectively, and longitudinal acoustic (LA) velocities decrease by 14% and 11%, respectively, along [100] and [010]. In addition, broadening of all phonon branches with increasing temperature can

Table 2 | Group velocity of acoustic phonons along the high-symmetry directions from experimental data, DFT results are listed in parenthesis.

Direction	T (K)	LA	TA$_1$	TA$_2$
		v_g (m s^{-1})		
[100]	100	3,658	2,101	1,709
	300	3,564	1,988	1,688
	DFT, relaxed	(2,508)	(1,817)	(1,696)
	486	3,310	1,843	1,666
	648	3,131	1,678	1,635
	DFT, QH* 700 K	(1,668)	(1,551)	(1,277)
[010]	100	4,111	2,402	1,995
	300	3,973	2,466	1,928
	DFT, relaxed	(3,545)	(2,407)	(1,674)
	486	3,857	2,375	1,830
	648	3,654	2,339	1,766
	DFT, QH* 700 K	(3,442)	(2,326)	(1,451)
[001]	100	–	1,796	2,031
	300	–	1,719	2,020
	DFT, relaxed	(3,248)	(1,836)	(2,559)
	486	–	1,714	1,874
	648	–	1,639	1,827
	DFT, QH* 700 K	(3,333)	(1,696)	(2,472)

Unavailable data are shown as '–'. *Quasiharmonic calculation for expanded volume at 700 K.

be seen in Fig. 2c–f, corresponding to suppressed phonon lifetimes (enhanced anharmonic phonon–phonon scattering rates).

Understanding the temperature dependence of the thermal conductivity requires taking into account both changes in the propagation velocities of quasiparticles, as well as changes in scattering rates (equation (1)). As discussed above, the temperature dependence of the group velocities is very strong in SnSe. This reflects a strong intrinsic temperature dependence of interatomic force constants, associated with temperature-dependent bonding. Such temperature-dependent group velocities have typically not been included in first-principles computations of thermal conductivity[18]. However, in the present case we estimate that this group-velocity softening alone (independently of increased scattering rates) could suppress κ_{lat} by over 20% between 300 and 700 K. In this respect, the precise temperature dependence of the measured κ_{lat} could exhibit a departure from the $1/T$ behaviour usually expected from scattering rates increasing with the Bose thermal occupation ($\sim T$ at high temperature), in the case of temperature-independent phonon dispersions. We note that the temperature dependence of dispersions (and thus v_g) also modifies the three-phonon interaction phase space, potentially cancelling part of the thermal occupation effect on scattering rates. The softening of the dispersions can be captured with temperature-dependent effective harmonic force constants,
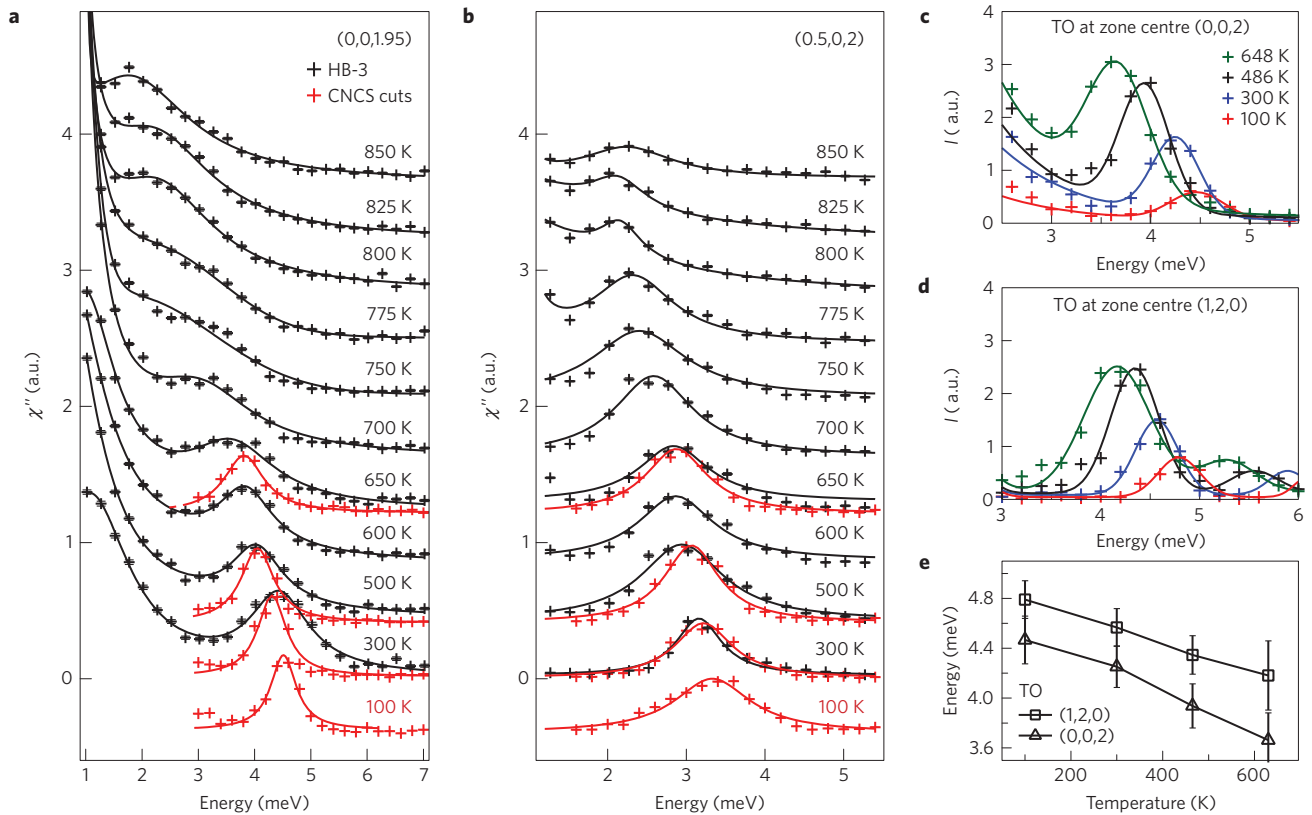
Figure 3 | Phonon spectra at constant-Q, showing a strong softening with increasing temperature. Constant-**Q** spectra for several low-energy phonon modes as a function of temperature, showing the pronounced temperature softening. Lines are fitted Lorentzian functions and most error bars are smaller than the symbol. **a**, Temperature dependence of spectra for the TO_c mode at $\mathbf{Q}=[0,0,1.95]$ from CNCS and HB3 measurements. The TO_c measurements on HB-3 were performed slightly off the zone centre to avoid the background from the intense Bragg peak. **b**, Same as **a** but for $\mathbf{Q}=[0.5,0,2]$. **c,d**, Spectra for c- and b-polarized TO modes at the zone centres [0,0,2] and [1,2,0], respectively, from CNCS data. **e**, Temperature dependence of zone-centre TO phonon energies at [0,0,2] and [1,2,0] with error bars indicating linewidths.

including the renormalization for both intrinsic anharmonic effects and for thermal expansion, by fitting the experimental dispersions (details in Supplementary Information). By performing such a procedure, we obtained strongly temperature-dependent effective (renormalized) harmonic force constants for the bonds d_2 and d_3. The renormalized harmonic force constants for d_2 (resp. d_3) decrease (resp. increase) as the bond becomes longer (resp. shorter) when the *Cmcm* phase is approached (see Supplementary Table III). These bonds are also identified as strongly anharmonic in our DFT simulations, as discussed below.

Our first-principles phonon calculations establish that the strong anharmonicity results from the local instability in the Sn environment, especially the Sn–Se d_2 and d_3 bonds along [011], which lead to large third-order interatomic force constants. The anharmonicity of the solid-state Hamiltonian can be quantified in a Taylor expansion of the interatomic potential:

$$V = V_0 + \frac{1}{2!}\Sigma_{i,j,\alpha,\beta}\Phi_{i,j}^{\alpha,\beta}u_i^\alpha u_j^\beta + \frac{1}{3!}\Sigma_{i,j,k,\alpha,\beta,\gamma}\Psi_{i,j,k}^{\alpha,\beta,\gamma}u_i^\alpha u_j^\beta u_k^\gamma + \cdots$$

where u_i^α is the atomic displacement at site $i=(l,\chi)$ (for atom χ in unit cell l) along direction α. $\Phi_{i,j}^{\alpha,\beta}$ are the second-order inter-atomic force constants. The third-order interatomic force constants in this expansion, $\Psi_{i,j,k}^{\alpha,\beta,\gamma}$, were computed from first principles using ShengBTE (ref. 20) and Phonopy (ref. 21). In the relaxation time approximation, the phonon gas thermal conductivity is given by

$$\kappa_{\text{lat}} = \frac{1}{3}\Sigma_{\mathbf{q}s}c_{\mathbf{q}s}v_{\mathbf{q}s}^2\tau_{\mathbf{q}s} \quad (1)$$

where $c_{\mathbf{q}s}$ is the heat capacity, $v_{\mathbf{q}s}$ the group velocity, and $\tau_{\mathbf{q}s}$ the scattering rate of the phonon mode of wavevector $\mathbf{q}$ and branch index s. The scattering rates can be obtained from perturbation theory[26] to first order in terms of the cubic IFCs:

$$\tau_{\mathbf{q}s}^{-1} = 2\Gamma_{\mathbf{q}s} = \frac{36\pi}{\hbar^2}\Sigma_{q_1,q_2,s_1,s_2}|V(\mathbf{q},\mathbf{q}_1,\mathbf{q}_2,s,s_1,s_2)|^2$$
$$\times (n_1+n_2+1)\{\delta(\omega_1+\omega_2-\omega_{\mathbf{q}s})-\delta(\omega_1+\omega_2+\omega_{\mathbf{q}s})\}$$
$$+ (n_2-n_1)\{\delta(\omega_1-\omega_2-\omega_{\mathbf{q}s})-\delta(\omega_1-\omega_2+\omega_{\mathbf{q}s})\} \quad (2)$$

with $n_1 = n(\omega_{\mathbf{q}_1 s_1}, T) \propto T$ the Bose occupation (likewise for n_2), where ω is the phonon frequency, and

$$V(\mathbf{q},\mathbf{q}_1,\mathbf{q}_2,s,s_1,s_2) = \frac{1}{6}\left(\frac{\hbar^3}{8\omega_1\omega_2\omega N}\right)^{1/2}$$
$$\times \sum_{l,l',k,k',k'',\alpha,\beta,\gamma}\Psi_{0,l,l'}^{\alpha,\beta,\gamma}e_\alpha(k|\mathbf{q}s)e_\beta(k'|\mathbf{q}_1 s_1)e_\gamma(k''|\mathbf{q}_2 s_2)$$
$$\times \left(\frac{1}{M_k M_{k'} M_{k''}}\right)^{1/2}e^{i(\mathbf{q}\cdot\mathbf{R}_{0,k}+\mathbf{q}_1\cdot\mathbf{R}_{l,k'}+\mathbf{q}_2\cdot\mathbf{R}_{l',k''})}\Delta(\mathbf{q}+\mathbf{q}_1+\mathbf{q}_2) \quad (3)$$

where $e(k|\mathbf{q}s)$ is the eigenvector, $\mathbf{R}$ is the atomic equilibrium position, and M_k is the atomic mass. From the first-principles cubic IFCs, the lattice thermal conductivity, κ_{lat}, was computed. Our detailed analysis of the third-order force constants and their contributions to the thermal transport shows how the anharmonicity arises from nonlinear restoring forces, owing to an
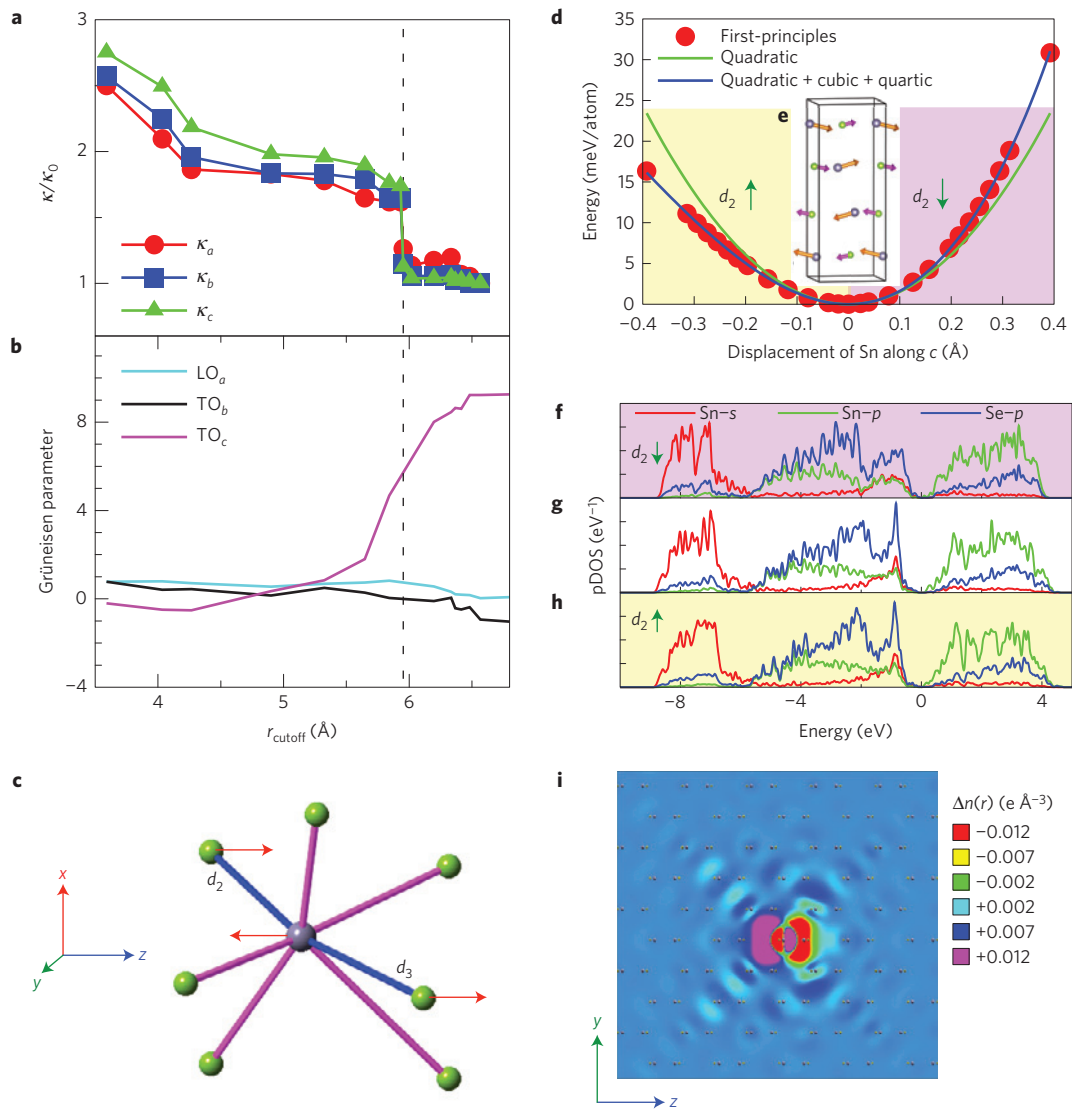
Figure 4 | First-principles calculations of phonon transport and anharmonicity. a, Convergence of the lattice thermal conductivity (relative change) of the *Pnma* phase of SnSe along the *a*, *b* and *c* crystallographic directions, with respect to the cutoff distance (r_{cutoff}) for the maximum interaction range of third-order force constants used in the anharmonic calculations. κ_0 is the thermal conductivity with the largest r_{cutoff} along each direction. **b**, Convergence of Grüneisen parameters (γ) versus r_{cutoff}, for zone-centre optical modes polarized along *a*, *b* and *c* ($E = 8.3$, 4.3 and 3.9 meV, respectively). The jump in κ_{lat} and γ occurs when the cutoff becomes large enough ($r_{cutoff} > 6$ Å) to include the strongly anharmonic triplets in the Sn 1NN coordination shell, as discussed in the text. **c**, Illustration of a strongly anharmonic triplet, $\Psi^{c,c,c}_{Sn,Se_2,Se_3}$. **d,e**, Anharmonic frozen-phonon potential (**d**) and displacement pattern (**e**) for the lowest-energy $TO_c(\Gamma)$ mode (*Pnma*). **f–h**, Orbital-projected electronic density of states (*Pnma* phase) in the structure at equilibrium and modulated by the TO_c phonon. **i**, Map of electron density change induced by the displacement (0.02 Å along *z*) of the central Sn atom in the *b–c* plane within 5 × 5 unit cells, with 3 unit cells along the *a*-direction. Oscillations along diagonals show long-range interactions in the *b–c* plane along the ⟨011⟩ directions.

asymmetric change of the electronic structure for motions of Sn atoms along *c*.

The cubic IFCs, $\Psi^{\alpha,\beta,\gamma}_{i,j,k}$, correspond to third-order derivatives of the potential energy with respect to displacements (α, β, γ) of triplets of atoms (i, j, k). Through a systematic investigation of the $\Psi^{\alpha,\beta,\gamma}_{i,j,k}$, we identified the non-degenerate triplets with largest third-order force constants. The triplets $\Psi^{c,c,c}_{Sn,Se_2,Se_3}$, $\Psi^{c,c,c}_{Se,Sn_2,Sn_3}$ and $\Psi^{c,a,a}_{Sn,Se_2,Se_4}$ are particularly large. All these include Sn motions along *c*, and motions of Se within the coordination shell. The first kind of triplet is illustrated in Fig. 4c. In this notation, the bond Sn–Se$_2$ is d_2 and the bond Sn–Se$_3$ is d_3. All these triplets have for the largest segment of the triangle, a value $d_0 \approx 6$ Å, which leads to a striking maximum anharmonicity as a function of interaction distance (Supplementary Fig. Va). This behaviour is compounded by the fact that the population of this kind of triplet is much larger than

any other (Supplementary Fig. Vb). Including the corresponding IFCs (that is, cutoff $d > d_0$) yields a strong suppression in thermal conductivity and an increase in Grüneisen parameter of the lowest-energy TO_c branch (at Γ), as shown in Fig. 4a,b. The large third-order force constant Ψ of these triplets, combined with the large triplet population, augments $|V(\mathbf{q}, \mathbf{q}_1, \mathbf{q}_2, s, s_1, s_2)|$ in equation (3), and therefore increases the scattering rates (equation (2)), leading to the striking suppression in the thermal conductivity (large drop at d_0 in Fig. 4a).

We note also that the distortion corresponding to $\Psi^{c,c,c}_{Se,Sn_2,Sn_3}$ matches the structural evolution of the unit cell from *Cmcm* to *Pnma* on cooling, and thus also indicates the role of anharmonic bonding in the structural phase transition. The distortion along *c* of this triplet overlaps strongly with the zone-centre optical phonon mode, $TO_c(\Gamma)$. On the other hand, the $LO_a(\Gamma)$ and $TO_b(\Gamma)$ modes

are rather insensitive to this interaction (Fig. 4b), as is expected because their polarization vectors are orthogonal and do not activate this cubic term. The strong TO_c anharmonicity is revealed in the distortion potential for the zone-centre TO_c vibration mode, as shown in Fig. 4d. The potential is asymmetric and strongly departs from the parabolic (harmonic) behaviour, indicating the nonlinear dependence of ionic forces on displacement amplitudes. This asymmetry is reflected in the electronic structure of the distorted structures, as discussed below. We also note that the strong anharmonicity for Sn vibrations along c probably contributes to the negative thermal expansion in this direction (Supplementary Fig. I). In addition to the strongly anharmonic bonding, the bilayer structure of the unit cell also plays an important role in the phonon–phonon interactions, by increasing the size of the three-phonon scattering phase space, through the band-folding described above.

The origin of the strong anharmonicity and off-centring of Sn atoms can be traced to the electronic structure. The p-orbitals of Se form a resonant network with large polarizabilities and long-range IFCs, leading to low zone-centre optical mode frequencies, and favouring the instability of the $Cmcm$ phase[27]. The symmetry-lowering transition from $Cmcm$ to $Pnma$ is akin to a second-order Jahn–Teller instability[28]. We computed the dielectric constant and Born effective charges with density-functional perturbation theory[29], and found abnormally large dielectric constants (23.3, 31.1, 27.0) along the a, b, c directions, indicating strong stereochemical activity[30,31]. For the low-T $Pnma$ phase, the Born effective charges are unusually large as well: (4.04, 4.90, 4.20) for Sn and (−4.04, −4.90, −4.20) for Se (in electron units, diagonal components—for full tensor see Supplementary Table IV), that is, double the conventional ionic charges, revealing a large polarizability of the electronic cloud. For the high-T $Cmcm$ phase, they are even larger: the dielectric constants are (23.7, 58.6, 39.4) and the Born effective charge tensor components (3.70, 6.20, 6.03) for Sn and the corresponding negative charge for Se, indicating larger electronic polarizability. We also find significant long-ranged force-constants components in the [011] directions, along the direction of Sn–Se (d_2) bonds (Supplementary Table III). These long-ranged interactions result from the long-ranged charge-density perturbations on atomic displacements, which are particularly extended along [011], as seen in Fig. 4i. These large polarizabilities and long-range forces are in agreement with the insight that resonant bonding of chalcogen p-states can lead to soft-mode instabilities[27].

The calculated orbital-projected electronic density of states (DOS) of the low-T structure shows that bonding states near the Fermi level are dominated by Se p-states, which form a broad band (∼6 eV wide) hybridized with the Sn s band and mediated by the Sn p-states (Fig. 4g). The Sn s-states are mainly confined 8 eV below the Fermi level, but also show a peak just below the top of the valence band, from hybridization with p-states (Sn $5s$ lone-pair formation from hybridization with apical Se1 p_x (ref. 28), pointing normal to the bilayers). Interestingly, we find that the DOS changes in an asymmetric way, with the distortion following the zone-centre TO_c vibration mode (Fig. 4e), similar to the frozen-phonon potential discussed above. As can be seen from Fig. 4h, when the distortion elongates d_2 and shortens d_3, the DOS changes little. However, the opposite distortion (d_2 decreases and d_3 increases) has a significant effect on the DOS (Fig. 4f), especially broadening the Sn s peak just below the top of the valence band.

Examination of the real-space electronic density reveals an isolated lobe around each Sn atom, characteristic of stereochemically active lone pairs, pointing towards the interlayer, in agreement with refs 28,30. This is shown in the electron density plots in Fig. 1c,f. The lone pair is active in both $Pnma$ and $Cmcm$ phases, and couples with the 1NN shell distortion at the transition, as it points opposite d_1 in $Cmcm$ and towards d_5 in $Pnma$. We note that the activity of the Sn lone pair was also observed in Mössbauer measurements[20].

The soft mode and off-centring of Sn atoms are thus understood from a combination of resonant p-bonding and Sn lone-pair activity causing a distortion of the local Sn coordination polyhedron. Our calculations of frozen-phonon potentials directly show how the changes in the electronic structure lead to nonlinear forces and a strong cubic term in the potential (Fig. 4d). Thus, the anharmonicity of phonon quasiparticles is directly related to the orbital instability via electron–phonon coupling.

Through a combination of INS measurements and first-principles simulations, we have shown that phonons in SnSe are strongly anisotropic and exhibit giant anharmonicity, associated with a soft-mode lattice instability driven by the resonantly bonding Se p-states and stereochemically active Sn lone pair. The anisotropic, ultralow thermal conductivity stems from the layered structure and strongly anharmonic phonons. Although structural phase transitions may impact longevity in thermoelectric devices, second-order transitions from soft modes, especially when confined to high temperatures, could mitigate these concerns. Thus, these results provide novel insights for the design and discovery of efficient thermoelectric materials, prompting a search for compounds with soft-mode lattice instabilities at very high temperatures, in which electronic symmetry breaking can favour nonlinear bonding. Our results also highlight the potential of layered metal chalcogenides for strongly anisotropic thermal management.

Methods

Methods and any associated references are available in the online version of the paper.

References

1. Snyder, G. J. & Toberer, E. S. Complex thermoelectric materials. *Nature Mater.* **7,** 105–114 (2008).
2. Minnich, A. J., Dresselhaus, M. S., Ren, Z. F. & Chen, G. Bulk nanostructured thermoelectric materials: Current research and future prospects. *Energy Environ. Sci.* **2,** 466–479 (2009).
3. Poudel, B. *et al.* High-thermoelectric performance of nanostructured bismuth antimony telluride bulk alloys. *Science* **320,** 634–638 (2008).
4. Biswas, K. *et al.* High-performance bulk thermoelectrics with all-scale hierarchical architectures. *Nature* **489,** 414–418 (2012).
5. Keppens, V. *et al.* Localized vibrational modes in metallic solids. *Nature* **395,** 876–878 (1998).
6. Koza, M. M. *et al.* Breakdown of phonon glass paradigm in La- and Ce-filled Fe$_4$Sb$_{12}$ skutterudites. *Nature Mater.* **7,** 805–810 (2008).
7. Christensen, M. *et al.* Avoided crossing of rattler modes in thermoelectric materials. *Nature Mater.* **7,** 811–815 (2008).
8. Ma, J. *et al.* Glass-like phonon scattering from a spontaneous nanostructure in AgSbTe$_2$. *Nature Nanotech.* **8,** 445–451 (2013).
9. Voneshen, D. J. *et al.* Suppression of thermal conductivity by rattling modes in thermoelectric sodium cobaltate. *Nature Mater.* **12,** 1028–1032 (2013).
10. Chiritescu, C. *et al.* Ultralow thermal conductivity in disordered, layered WSe$_2$ crystals. *Science* **315,** 351–353 (2007).
11. Rhyee, J.-S. *et al.* Peierls distortion as a route to high thermoelectric performance in In$_4$Se$_{3-\delta}$ crystals. *Nature* **459,** 965–968 (2009).
12. Delaire, O. *et al.* Giant anharmonic phonon scattering in PbTe. *Nature Mater.* **8,** 614–619 (2011).
13. Nielsen, M. D., Ozolins, V. & Heremans, J. P. Lone pair electrons minimize lattice thermal conductivity. *Energy Environ. Sci.* **6,** 570–758 (2013).
14. Li, C. W. *et al.* Phonon self-energy and origin of anomalous neutron scattering spectra in SnTe and PbTe thermoelectrics. *Phys. Rev. Lett.* **112,** 175501 (2014).
15. Zhao, L.-D. *et al.* Ultralow thermal conductivity and high thermoelectric figure of merit in SnSe crystals. *Nature* **508,** 373–377 (2014).
16. Chen, C.-L., Wang, H., Chen, Y.-Y., Day, T. & Snyder, G. J. Thermoelectric properties of p-type polycrystalline SnSe doped with Ag. *J. Mater. Chem. A* **2,** 11171–11176 (2014).
17. Sassi, S. *et al.* Assessment of the thermoelectric performance of polycrystalline p-type SnSe. *Appl. Phys. Lett.* **104,** 212105 (2014).
18. Carrete, J., Mingo, N. & Curtarolo, S. Low thermal conductivity and triaxial phononic anisotropy of SnSe. *Appl. Phys. Lett.* **105,** 101907 (2014).

19. Klemens, P. G. in *Solid State Physics, Advances in Research and Applications* Vol. 7 (eds Seitz, F. & Turnbull, D.) 1–98 (Academic Press, 1958).
20. Li, W., Carrete, J., Katcho, N. A. & Mingo, N. ShengBTE: A solver of the Boltzmann transport equation for phonons. *Comput. Phys. Commun.* **185,** 1747–1758 (2014).
21. Togo, A., Oba, F. & Tanaka, I. First-principles calculations of the ferroelastic transition between rutile-type and $CaCl_2$-type SiO_2 at high pressures. *Phys. Rev. B* **78,** 134106 (2008).
22. Chattopadhyay, T., Pannetier, J. & Von Schnering, H. G. Neutron diffraction study of the structural phase transition in SnS and SnSe. *J. Phys. Chem. Solids* **47,** 879–885 (1986).
23. von Schnering, H. G. & Wiedemeier, H. The high temperature structure of α-SnS and β-SnSe and the B16-to-B33 type λ-transition path. *Z. Kristallogr.* **156,** 143–150 (1981).
24. Cochran, W. Crystal stability and the theory of ferroelectricity. *Adv. Phys.* **9,** 387–423 (1960).
25. Pawley, G. S., Cochran, W., Cowley, R. A. & Dolling, G. Diatomic ferroelectrics. *Phys. Rev. Lett.* **17,** 753–755 (1966).
26. Cowley, R. A. Anharmonic crystals. *Rep. Prog. Phys.* **31,** 123–166 (1968).
27. Lee, S. *et al.* Resonant bonding leads to low lattice thermal conductivity. *Nature Commun.* **5,** 3525 (2014).
28. Tremel, W. & Hoffmann, R. Tin sulfide, $(Te_2)_2I_2$, and related compounds: Symmetry-controlled deformations in solid-state materials. *Inorg. Chem.* **26,** 118–127 (1987).
29. Wu, X., Vanderbilt, D. & Hamann, D. R. Systematic treatment of displacements, strains, and electric fields in density-functional perturbation theory. *Phys. Rev. B* **72,** 035105 (2005).
30. Orgel, L. E. The stereochemistry of B subgroup metals. Part II. The inert pair. *J. Chem. Soc.* **1959,** 3815–3819 (1959).
31. Waghmare, U. V., Spaldin, N. A., Kandpal, H. C. & Seshadri, R. First-principles indicators of metallicity and cation off-centricity in the IV–VI rocksalt chalcogenides of divalent Ge, Sn, and Pb. *Phys. Rev. B* **67,** 125111 (2003).
32. Chandrasekhar, H. R., Humphreys, R. G., Zwick, U. & Cardona, M. Infrared and Raman spectra of the IV–VI compounds SnS and SnSe. *Phys. Rev. B* **15,** 2177–2183 (1977).

Acknowledgements

Author contributions

C.W.L. and O.D. performed the neutron scattering measurements with help from S.C., T.H. and G.E. J.H. and D.B. performed the first-principles simulations and lattice dynamics modelling. A.F.M. synthesized the samples. O.D., C.W.L. and J.H. wrote the manuscript and all authors commented on it. O.D. supervised the project.

Additional information

Supplementary information is available in the online version of the paper. Reprints and permissions information is available online at www.nature.com/reprints. Correspondence and requests for materials should be addressed to O.D.

Competing financial interests

The authors declare no competing financial interests.

Methods

Sample synthesis. Single crystals of SnSe were synthesized with high-purity Sn and Se (Alfa Aesar, 99.999%), using a modified Bridgman technique. The elements were sealed in a fused silica ampoule and slowly heated to 500 °C, held for 10 h, then held at 950 °C for an additional 10 h before cooling. The resulting polycrystalline material was then crystallized in a tapered, fused silica ampoule while cooling at 0.4–0.5 °C h^{-1} from the melt to approximately 830 °C, followed by a 24 h anneal before cooling to 500 °C and shutting off the furnace. The quality of crystals was checked with X-ray and neutron diffraction. Typical crystals used in neutron scattering experiments had a mass of approximately 8 g.

Inelastic neutron scattering measurements. Inelastic neutron scattering (INS) measurements were performed on single crystals with the CNCS spectrometer at the Spallation Neutron Source (SNS; ref. 33). The measurements were performed with incident energies $E_i = 12$ meV, and at several different temperatures (100, 300, 486 and 648 K). Several crystals were used, oriented with either the [010] or [001] axis vertical, and data were collected for multiple orientations (rotations about the vertical) over a wide range of angles. The data were subsequently combined to generate the four-dimensional scattering function, $S(\mathbf{Q}, E)$, using standard software[34], and then 'sliced' along selected **Q**-directions to produce two-dimensional views, some of which are shown in Fig. 2 and Supplementary Fig. Ia. One-dimensional 'cuts' were also taken along the energy axis to obtain phonon spectra at specific **Q**-points. The phonon energies measured at the zone centre compare well with the Raman/IR results from the literature, as shown in Supplementary Table I. The phonon group velocities and mode Grüneisen parameters obtained from fitting the phonon dispersions in $S(\mathbf{Q}, E)$ are shown in Supplementary Table III.

Further triple-axis measurements were performed with thermal neutrons on the HB-3 spectrometer at the High Flux Isotope Reactor (HFIR), with the [010] axis vertical, for temperatures at 100, 300, 500, 600, 650, 700, 750, 775, 800, 825 and 850 K. The HB-3 measurements were performed using the PG002 monochromator and analyser, with a constant final energy $E_f = 14.7$ meV, and collimation settings of 48′–40′–40′–90′. The HB-3 experiment focused on transverse optical phonons near the centre of several Brillouin zones (data near (0,0,2) are shown in Fig. 3). The spectra for phonons were refined to extract the phonon energy and linewidth by computing the convolution of the instrument resolution function with a Lorentzian function as implemented in the software Reslib (ref. 35). Although the data from CNCS provided more extensive coverage of **Q** space, the HB-3 measurements enabled detailed studies of the temperature dependence of phonons. Additional measurements (lattice parameters) were performed with the Cold Neutron Triple-Axis Spectrometer (CTAX) at the High Flux Isotope Reactor (HFIR) using the same crystals. The measurements were performed using the PG002 monochromator and analyser, with a constant final energy $E_f = 5.0$ meV, and collimation settings of open–open–80–open.

First-principles simulations. All of our calculations were performed in the framework of density-functional theory (DFT) as implemented in the Vienna Ab initio simulation package (VASP; refs 36–38) with a plane-wave cutoff of 500 eV. We used both the local-density approximation (LDA; ref. 39) and the generalized gradient approximation (GGA; ref. 40), in both cases making use of the projector-augmented-wave (PAW) potentials, explicitly including four valence electrons for Sn ($5s^2$ $5p^2$) and six valence electrons for Se ($4s^2$ $4p^4$). We used experimental structures[41] as starting configurations and relaxed the lattice parameters and atomic positions until all atomic force components were smaller than 1 meV Å^{-1}. The results are shown in Table 2. The harmonic phonon dispersion calculations were performed with VASP and Phonopy. We used $3 \times 5 \times 5$ supercells in the phonon calculations. On the basis of the convergence studies, we used $6 \times 12 \times 12$ and $2 \times 4 \times 4$ Monkhorst–Pack electronic k-point meshes for the unit cell and supercell, respectively. The LDA was used more extensively, as it achieved better agreement between the predicted phonon dispersions and our INS measurements. We note that the calculated Born effective charges are much larger than the nominal values suggested by the number of valence electrons (Supplementary Table V).

We also calculated the phonon transport properties in SnSe from first principles based on the Boltzmann transport equation (BTE) formalism using ShengBTE (ref. 20). The second- and third-order interatomic force constants were computed in the $3 \times 5 \times 5$ supercells containing 600 atoms. Some of the results for the thermal conductivity calculations are shown in Fig. 4a. We note that the convergence of the thermal conductivity with interaction range is slow, as described in the main text, and was carefully investigated in the present study.

To compare with the INS measurements, the dynamical structure factor was computed from the first-principles phonon dispersions and polarization vectors ($\epsilon_{d,s}$) as follows[42]:

$$S(\mathbf{Q}, E) \propto \sum_s \sum_\tau \frac{1}{E_s} \left| \sum_d \frac{\overline{b_d}}{\sqrt{M_d}} e^{(W_d + i\mathbf{Q} \cdot \mathbf{r}_d)} (\mathbf{Q} \cdot \epsilon_{ds}) \right|^2$$
$$\times \langle n_s + 1 \rangle \delta(E - E_s) \delta(\mathbf{Q} - \mathbf{q} - \tau)$$

where s, τ and d denotes the branch index, reciprocal lattice vector and atom index in the unit cell, respectively, and $\overline{b_d}$, $\mathbf{r}_d$ and M_d are the coherent neutron scattering length, position and atomic mass for atom d. The Debye–Waller factor, W_d, was calculated assuming the atomic mean-square displacements are isotropic. The result was convolved with a 4-dimensional Gaussian instrument resolution function, $R(\mathbf{Q}, E)$. A constant Q resolution, of comparable width to the bin sizes of $S(\mathbf{Q}, E)$ integration, and a known energy-dependent energy resolution were used. The results are in good agreement with the INS measurement, as can be seen in Fig. 2 and Supplementary Fig. I, validating the first-principles phonon calculations.

Temperature-dependent effective harmonic force constants. Phonon dispersions provide information in reciprocal space. To study the origin of phonon softening in real space, we examined the behaviour of Born–von Karman (BvK) force constants as a function of temperature. Here, we optimized the BvK force constants (F11, F22 and F33) corresponding to bonds d_2 and d_3 using Phonopy[26], in-house Python routines, and the Dakota optimization package[43] for a $3 \times 5 \times 5$ supercell, optimized against experimental data at different temperatures. The force constants F11, F22 and F33 yield the forces on a Sn atom along the a, b and c axes, with respect to unit displacement of the Se atom (d_2 or d_3 bond) along the a, b and c axis. The symmetry of the space group, including image effects at the edges of the supercell, was enforced during every step of the optimization process. We tested the 'nl2sol', 'coliny_pattern_search' and 'moga' optimization routines implemented in Dakota. The 'nl2sol' solver resulted in significantly lower error norms and was used for further optimizations. We constrained the optimization against experimental phonon frequencies of one TO mode at (0,0,0), and one TA mode at each of (0,0.25,0), (0,0.25,0.25) and (0,0,0.5) q-points. The convergence tolerance was set to a value of 10^{-4}. Furthermore, the sensitivity analysis indicated the error in calculated BvK force constants to be of the order of 0.05 eV Å^2. The optimized BvK force constants are shown in Supplementary Table IV. The results reveal strongly temperature-dependent effective force constants for both the d_2 and d_3 bonds. As temperature increases in the *Pnma* phase, the d_2 and d_3 bond lengths become closer, until they become identical in the high-symmetry *Cmcm* phase (mirror plane). This implies that the magnitude of BvK force constants ($\{F11^2 + F22^2 + F33\}^{1/2}$) must also become identical (individual components should comply with the symmetry of the *Cmcm* phase). The trend obtained from our optimized temperature-dependent force constants is thus compatible with this expectation.

References
33. Ehlers, G., Podlesnyak, A. A., Niedziela, J. L., Iverson, E. B. & Sokol, P. E. The new cold neutron chopper spectrometer at the Spallation Neutron Source: Design and performance. *Rev. Sci. Instrum.* **82,** 085108 (2011).
34. Arnold, O. *et al.* Mantid—Data analysis and visualization package for neutron scattering and μSR experiments. *Nucl. Instrum. Methods A* **764,** 156–166 (2014).
35. Zheludev, A. ResLib 3.4 software (Oak Ridge National Laboratory, 2007); http://www.neutron.ethz.ch/research/resources/reslib
36. Kresse, G. & Furthmüller, J. Efficiency of *ab-initio* total energy calculations for metals and semiconductors using a plane-wave basis set. *Comput. Mater. Sci.* **6,** 15–50 (1996).
37. Kresse, G. & Hafner, J. J. *Ab initio* molecular dynamics for liquid metals. *Phys. Rev. B* **47,** 558–561 (1993).
38. Kresse, G. & Furthmüller, J. Efficient iterative schemes for *ab initio* total-energy calculations using a plane-wave basis set. *Phys. Rev. B* **54,** 11169–11186 (1996).
39. Perdew, J. P. & Zunger, A. Self-interaction correction to density-functional approximations for many-electron systems. *Phys. Rev. B* **23,** 5048–5079 (1981).
40. Perdew, J. P., Burke, K. & Ernzerhof, M. Generalized gradient approximation made simple. *Phys. Rev. Lett.* **77,** 3865–3868 (1996).
41. Adouby, K., Pérez-Vicente, C., Jumas, J. C., Fourcade, R. & Touré, A. A. Structure and temperature transformation of SnSe. Stabilization of a new cubic phase Sn$_4$Bi$_2$Se$_7$. *Z. Kristallogr.* **213,** 343–349 (1998).
42. Squires, G. *Introduction to the Theory of Thermal Neutron Scattering* (Cambridge Univ. Press, 1978).
43. Adams, B. M. *et al.* DAKOTA, A Multilevel Parallel Object-Oriented Framework for Design Optimization, Parameter Estimation, Uncertainty Quantification, and Sensitivity Analysis Version 5.0 user's manual. Sandia Technical Report SAND 2010-2183 (2013).